Experimental and computational evaluation of dipeptidyl peptidase III inhibitors based on quinazolinone-Schiff's bases

Dejan Agić[1*], Maja Karnaš[1], Sanja Tomić[2], Mario Komar[3], Zrinka Karačić[2], Vesna Rastija[1], Drago Bešlo[1], Domagoj Šubarić[1] and Maja Molnar[3].

[1]Faculty of Agrobiotechnical Sciences Osijek, Josip Juraj Strossmayer University of Osijek, 31000 Osijek, Croatia

[2]Divison of Organic Chemistry and Biochemistry, Ruđer Bošković Institute, 10000 Zagreb, Croatia

[3]Faculty of Food Technology Osijek, Josip Juraj Strossmayer University of Osijek, 31000 Osijek, Croatia

*Corresponding author: dejan.agic@fazos.hr

Abstract: Dipeptidyl peptidase III (DPP III) is a zinc-dependent enzyme that sequentially hydrolyzes biologically active peptides by cleaving dipeptides from their N-termini. Although its fundamental role is not been fully elucidated, human DPP III (hDPP III) has been recognized in several pathophysiological processes of interest for drug development. In this article 27 quinazolinone-Schiff's bases were studied for their inhibitory activity against hDPP III combining an in vitro experiment with a computational approach. The biochemical assay showed that most compounds exhibited inhibitory activity at the 100 μM concentration. The best QSAR model included descriptors from the following 2D descriptor groups: information content indices, 2D autocorrelations, and edge adjacency indices. Five compounds were found to be the most potent inhibitors with IC_{50} values below 10 μM, while molecular docking predicted that these compounds bind to the central enzyme cleft and interact with residues of the substrate binding subsites. Molecular dynamics simulations of the most potent inhibitor (IC_{50}=0.96 μM) provided valuable information explaining the role of PHE109, ARG319, GLU327, GLU329, and ILE386 in the mechanism of the inhibitor binding and stabilization. This is the first study that gives insight into quinazolinone-Schiff's bases binding to this metalloenzyme.

Keywords: dipeptidyl peptidase III, inhibitor, molecular modeling, quinazolinone-Schiff's bases

1. Introduction

Dipeptidyl peptidase III (DPP III; EC 3.4.14.4) is a zinc enzyme belonging to the metallopeptidase family M49, which sequentially hydrolyses a number of biologically active peptides by cleaving dipeptides from their N-termini (Chen & Barrett, 2004; Baršun et al., 2007). Family M49 has been recognized as a distinct group based on the unique structural motifs HEXXGH and EEXR (K)AE(D) which are necessary for the binding of zinc cation (Zn^{2+}) to the enzyme active site and catalytic activity. Zinc cation is responsible for the activation of a water molecule that in the hydrolysis act as a nucleophile and attack the carbonyl carbon atom of the scissile peptide bond (Chen & Barrett, 2004). Insight into the crystal structure of human DPP III (h DPP III) without ligand showed that the molecule has an elongated shape (50 x 151 x 54 Å) with two domains separated by a wide cleft (Figure 1 left). The upper domain was mostly made of α-helix and the lower domain with a mixed α-helices and β-sheets. The active site with the zinc cation is located in the lower part of the upper domain and is directed towards the inter-domain cleft (Bezerra et al., 2012). According to previous experimental and computational approaches, it has been shown that the enzyme can be transformed from an extended („open“) form (Figure 1 left) into a compact („closed“) form (Figure 1 right), while the conformation of both protein domains has been preserved (Bezerra et al., 2012; Kumar et al., 2016; Tomić et al., 2012; Tomić et al., 2015). In addition, MD simulations of the extended form of hDPP III have shown that in solution protein is abundant in different conformations whose „semi-closed“ form (Figure 1 middle) is the most presented (Tomić et al., 2012).

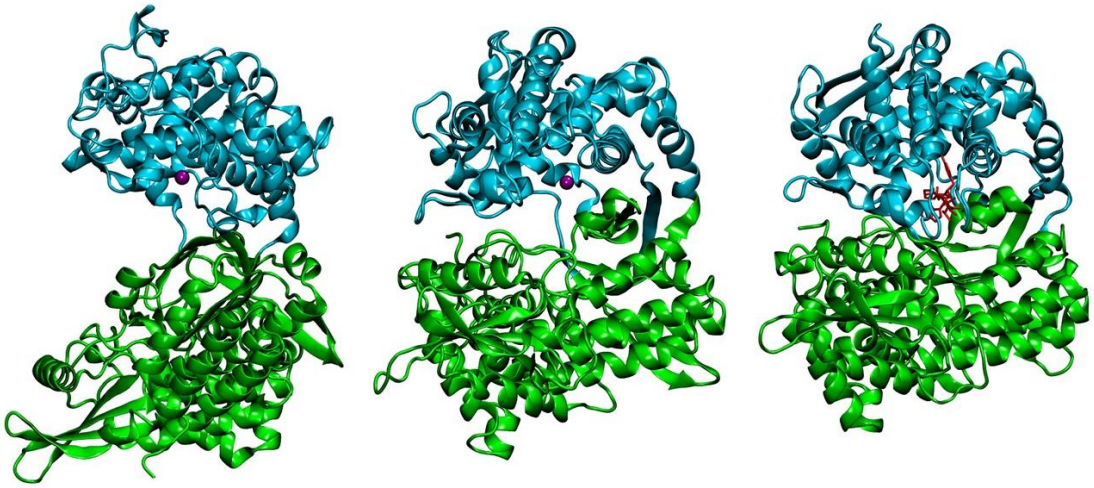

Figure 1. Different forms of human DPP III structures: (left) „open form“ (PDB code: 3FVY), (middle) „semi-closed form“, and (right) „closed form“ in complex with pentapeptide tynorphin (PDB code: 3T6B). Two domains of the DPP III protein are shown in cyan and green, the zinc cation is represented as a purple sphere, while the red stick model shows tynorphin. Color figure can be viewed in the online issue.

To date, hDPP III is a very well defined member of M49 family, in terms of biochemistry, structural biology and computational chemistry (Chen & Barrett, 2004; Baršun et al., 2007; Bezerra et al., 2012; Karačić et al., 2012; Kumar et al., 2016; Tomić et al., 2014; Tomić & Tomić, 2022). Even though its fundamental role has not been fully elucidated, DPP III is implicated in the final steps of intracellular protein catabolism (Abramić et al., 1988) and various physiological processes, including blood pressure regulation (Pang et al., 2016; Jha et al., 2020) pain modulation (Sato et al., 2003) oxidative stress response and regulation of the Nrf2/KEAP1 signaling pathway (Liu et al., 2007; Matić et al., 2020). Because it is involved in pathological processes such as cataractogenesis (Zhang et al., 2001) and progression of some cancers (Šimaga et al., 1998; Šimaga et al.,2003; He et al., 2010; Lu et al., 2017; Prajapati et al., 2016) hDPP III become an interesting target for drug development.

Quinazolinone nucleus is an important heterocyclic scaffold found in various biologically active natural products, synthetic compounds, pharmaceutical drugs and agrochemicals (Radwan & Alanazi, 2020). Schiff bases are a versatile family of compounds that carry imine or azomethine functional groups and exhibit a wide range of biological activities (Kajal et al., 2013). Thus, Schiff bases containing a quinazolinone core possess various biological activities such as antibacterial, antidiabetic, anti-inflammatory, and cytotoxic activity (Hricovíniová et al., 2018; Rakesh et al., 2015). Furthermore, both quinazolinone and Schiff bases derivatives have exhibited promising activity against some matrix metalloproteinases (Li et al., 2008; Harney et al., 2012). Previously, we have shown that heterocyclic compounds such as polyphenols (Agić et al., 2017; Blagojević et al., 2021) and coumarins (Agić et al., 2021) have a potential to inhibit hDPP III by binding to a hydrophobic pocket and forming hydrogen bonds through OH groups with enzyme active site residues. The activities mentioned above encouraged us to experimentaly evaluate the effect of an unexplored class of heterocyclic compounds against hDPP III.

In this study we report the discovery of quinazolinone Schiff bases, synthesized and characterized earlier by Komar et al., 2021, that inhibit hDPP III at micromolar concentration. Computational techniques were used to describe the molecular basis of the observed activity of the most potent inhibitors.

2. Material and Methods

2.1. Heterologous expression and purification of recombinant human DPP III

C-terminally truncated human DPP III was expressed and purified as described previously (Kumar et al., 2016). In brief, C-terminal HIS-tagged recombinant human DPP III was expressed in *E. coli* BL21-CodonPlus (DE3)-RIL cells (Agilent). Overexpression was induced by 0.25 mM isopropyl-b-D-1-thiogalactopyranoside (IPTG, Fermentas) and the cells were grown 20 hours at 18 °C and 130 rpm. Obtained bacterial cells were lysed by a combination of lysozyme lysis and sonication, then treated with DNase I and centrifuged at 4000g for 15 minutes to precipitate the cell debris. The lysate was purified by affinity chromatography on Ni-NTA column (5 mL prepacked His-trap FF, GE Healthcare). All fractions with hDPP3 were pooled and incubated with TEV protease to remove the HIS-tag. hDPP III was recovered using flow-through affinity chromatography (TEV protease is His-tagged), and additionally purified on a 16/60 Superdex-200 gel-filtration column (GE Healthcare). Fractions with hDPP III were pooled and desalted on PD-10 columns (GE Healthcare). Purified protein in 20 mM Tris HCl buffer pH = 7.4 were stored at -80 °C until use.

2.2. Human DPP III activity assay and IC_{50} determination

Recombinant hDPP III (1.1 nM) was preincubated with quinazolinone-Schiff's bases (100 μM) first for 5 min at 27 °C and then for 5 min at 37 °C in 50 mM Tris-HCl buffer, pH 7.4. The enzymatic reaction was started with ARG_2-2NA (40 μM) as a substrate, and after the 15 min incubation at 37 °C in a water bath, the reaction was stopped and the absorbance was measured using the spectrophotometric method described before (Špoljarić et al., 2009). The stock solutions (8 mM) of quinazolinone-Schiff's bases were prepared daily in dimethyl sulfoxide and diluted with 50 mM Tris-HCl buffer, pH 7.4 before assay of enzymatic activity.

Percentage enzyme inhibition (% inh.) was calculated by comparing the enzymatic activity without (control activity), and with inhibitor (inhibited activity) using the following formula:

$$\% \text{ inh.} = [(\text{control activity} - \text{inhibited activity}) / (\text{control activity})] \times 100 \quad \text{Eq1}$$

Compounds that showed strongest inhibition (% inh. ≥ 90) were subjected to further IC_{50} determination. The percentage of enzyme inhibition under at least 9 different concentration gradients (increasing compound concentrations from 0.05 to 100 μM) were imported into GraphPad Prism 5 software (GraphPad) to calculate IC_{50} values of the compounds using non-linear regression analysis from the mean inhibitory value of three replicates.

2.3. Computational study of hDPP III inhibitors

2.3.1. QSAR analysis

3D structures of 27 quinazolinone Schiff bases, together with 3-aminoquinazolinone, were drawn in Avogadro 1.2.0. (Hanwell et al., 2012) and optimized by Spartan '08 software (Spartan '08), using the molecular mechanics force field (MM+) (Hocquet et al., 1998) and subsequently the semiempirical PM3 method (Stewart, 1989). The molecular structures were optimized using the Polak-Ribiere algorithm until the root mean square gradient (RMS) was 0.001 kcal/mol per Å.

Descriptor calculation for the optimized compounds was performed with Parameter Client (Virtual Computational Chemistry Laboratory, an electronic remote version of the Dragon program) (Tetko et al., 2005). Experimentally obtained values of hDPP III inhibition percentages were expressed as logarithmic values in order to normalize their distribution, and used as response values. The generation and validation of QSAR models was performed in QSARINS 2.2.4 (Gramatica et al., 2013). Constant and semi-constant descriptors, i.e., descriptors with a constant value for more than 85 % of compounds and descriptors that were too intercorrelated (> 95%) were rejected by QSARINS. The final number of descriptors after the reduction was 503. A genetic algorithm (GA) was used to generate the best model, and the number of descriptors in the multiple linear regression (MLR) equation was limited to three. Concerning the limited number of compounds (28), the set was not split into the training and test, therefore the generated models are not predictive.

All generated models were validated by the internal cross-validation performed using the "leave-one-out" (LOO) and Y-scrambling method (Gramatica et al., 2013). Evaluation criteria taken into consideration were: coefficient of determination (R^2), adjusted coefficient of determination (R^2_{adj}), cross-validated correlation coefficient (Q^2_{LOO}), inter-correlation among descriptors (K_{xx}), the difference of the correlation among the descriptors and the descriptors plus the responses (ΔK), the standard deviation of regression (s), Fisher ratio (F), root-mean-square error ($RMSE_{tr}$); LOO cross-validated root-mean-square error ($RMSE_{cv}$), concordance correlation coefficient (CCC_{tr}), LOO cross-validation concordance correlation coefficient (CCC_{cv}), mean absolute error of the training set (MAE_{tr}), mean absolute error of the internal validation set (MAE_{cv}). Y-randomization test was performed to check the robustness of models, providing R^2_{Yscr}, Q^2_{Yscr} and $RMSE_{AV\ Yscr}$ values (Gramatica, 2007). Williams plot was used to identify the possible outliers and compounds out of the warning leverage (h^*) in a model. The warning leverage is defined as $3p'/n$ (n is the number of training compounds, and p' the number

of model adjustable parameters) (Eriksson et al., 2003). Compounds having values of standardized residuals higher than two standard deviation units were deemed as outliers.

2.3.2. Model setup

The initial model for docking and MD simulations was built using the semi-closed conformation of hDPP III obtained earlier (Tomić et al., 2012) by MD simulations of the structure available in the Protein Data Bank (PDB code: 3FVY, resolution 1.9 Å), since it has been proved that this is the most preferable enzyme form in water solution (Tomić et al., 2015). All ARG and LYS residues are positively charged (+1) while all ASP and GLU residues are negatively charged (-1), as expected under the physiological conditions. To search for the best pose of the five most active compounds to the enzyme active site AutoDock Vina 1.1.2 was used (Trott & Olson, 2010). The docking site for these five compounds on hDPP III was defined by cubical grid box with dimensions $80 \times 80 \times 80$ Å^3 and the center placed on the Zn^{2+}. Docking was done with the standard grid box spacing of 0.375 Å and 20 conformations were generated. The complex with the best AutoDock Vina docking score was chosen for the productive MD simulations. Parameterization of the complex structure was performed by the AMBERTools16 modules *antechamber* and *tleap* using General Amber Force Field (GAFF) (Wang et al., 2004) and ff14SB (Maier et al., 2015) force fields to parameterize the ligand and the protein, respectively. For the zinc cation, Zn^{2+}, new hybrid bonded-nonbonded parameters were derived from our previous work (Tomić, 2019). The complex was dipped into the truncated octahedral box filled with TIP3P water molecules with a margin distance of 11 Å. To neutralize the system, added 24 Na^+ ions were placed in the vicinity of charged amino acids at the protein surface.

2.3.3. Dynamics simulations

The resulting system, consisting of ~73 000 atoms (~20 500 molecules of water), were simulated using periodic boundary conditions wherein the electrostatic interactions were calculated using the particle-mesh Ewald method. Prior to the MD simulations, the solvated complex was energy-minimized in three cycles with different restraints. In the first cycle 1 500 steps of minimization were performed, where the first 470 steps were of the steepest descent method, and the rest was the conjugate gradient. Both the protein atoms and the zinc cation were constrained using a harmonic potential of force constant 32 kcal/(mol Å^2), to equilibrate water molecules. In the second cycle 2 500 steps were performed and only the first 470 steps of steepest descent were used. The zinc cation and protein backbone were constrained with 32 kcal/(mol Å^2). Finally, in the third cycle, the same number of minimization steps was as in the first cycle, and both protein backbone and zinc cation were constrained with 10 and 32

kcal/(mol $Å^2$), respectively. Afterward, the minimized system was heated from 0 to 300 K during 30 ps using a canonical ensemble (NVT), and then equilibrated 80 ps during which the initial constraints on the protein and the metal ion were used. This was followed by another equilibration stage of 100 ps, during which the initial constraints on the protein and the metal ion were removed and the water density was adjusted. The time step during the periods of heating and the water density adjustment was 1 fs. The equilibrated system was then subjected to 210 ns of the productive MD simulations at constant temperature and pressure (300 K and 1 atm) using the NPT ensemble, without any constraints. The temperature was held constant using Langevin dynamics with a collision frequency of 1 ps^{-1}, and the Berendsen barostat respectively. Bonds involving hydrogen atoms were constrained using the SHAKE algorithm (Ryckaert et al., 1977). Simulations of the complex were performed within the AMBER16 software package (Case et al., 2016). The time step used for the productive MD simulations was set to 2 fs and the trajectory files were collected every 10 ps for the subsequent analysis. Trajectory analysis was performed by the CPPTRAJ module from the AmberTools16 program package and examined visually using Discovery Studio Visualizer, version 20.1.0.19295 (Dassault Systèmes BIOVIA) and VMD 1.9.3 (Humphrey et al., 1996) software.

3. Results and Discussion

3.1. *In vitro* DPP III inhibitory activity

In the current study 27 quinazolinone Schiff bases, prepared from 3-amino-2-methylquinazolin-4(3H)-one and substituted aromatic aldehydes, were studied for their effective inhibition of hDPP III. Most of the tested compounds inhibited (Table 1) enzyme at a concentration of 100 μM, but significant differences in their potency were observed, such that the percentage of inhibition (% inh.) value ranged from 2.4 to 97.4. The strongest inhibition (% inh. ≥ 90) has been determined with compounds **1**, **3**, **8**, **23**, and **25,** all exhibiting IC_{50} values below 10 μM (Table 1 and Figure 2). A slightly lower inhibition (% inh. ≥ 80 to <90) has been observed for compounds **6**, **14**, and **20**, while compounds **2**, **4**, **5**, **16**, **17**, **19**, **22**, **24**, and **26** have shown moderate inhibition (% inh. ≥ 50 to <80). Compounds **9**-**13**, **18**, **21**, and **27**, showed a mild inhibition (% inh. ≥ 20 to <50) whereas compounds **15** and **28** have shown weak inhibitory effect. Compound **7** was not active at all towards hDPP III (Table 1).

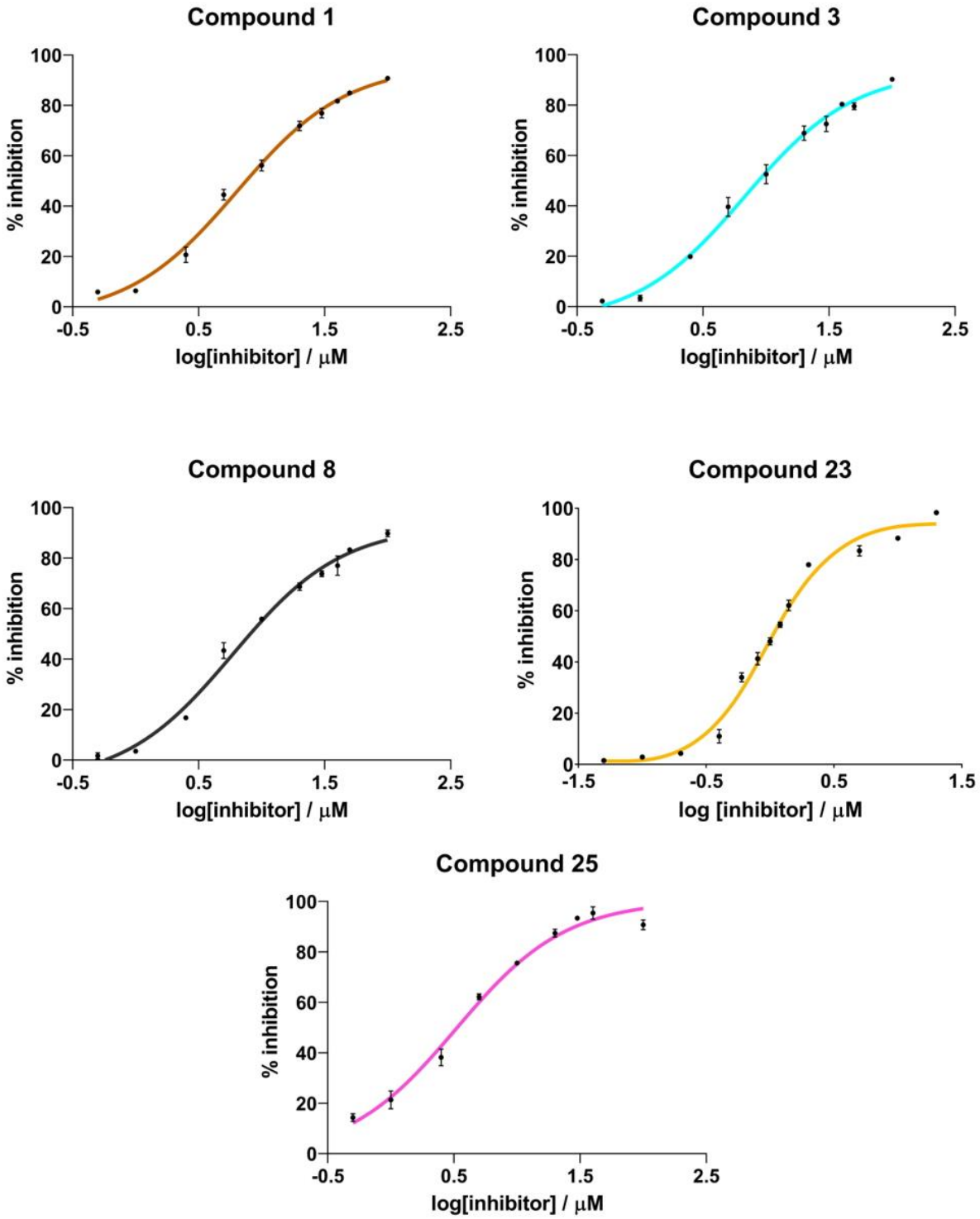

Figure 2. Graphs used for IC_{50} value determinations of compounds **1**, **3**, **8**, **23** and **25** against hDPP III. Dose-response data points represent the mean value ± SD of three replicates. Color figure can be viewed in the online issue.

Table 1. Structures of analysed compounds, values of experimentally determined inhibition of hDPP III (at 100 μM concentration of compounds) and calculated logarithmic values of the % inhibition of hDPP III.

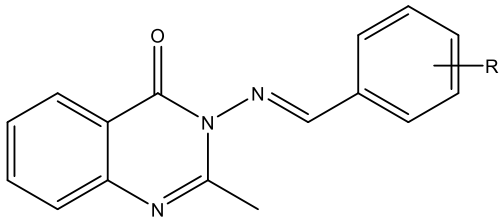

Compound	R	inh. (%)*	log (% inh.) exp.	log (% inh.) calc.**
1	2,4-$(OH)_2$	90.8±0.6 (7.73±0.09)	1.96	2.10
2	2-OH-3-OC_2H_5	61.3±0.8	1.79	1.73
3	2-OH	90.3±0.2 (8.70±0.08)	1.96	2.02
4	2-Cl	64.3±0.2	1.81	1.81
5	2-OH-5-Br	52.5±0.5	1.72	1.89
6	2,5-$(OCH_3)_2$	83.9±0.3	1.92	1.62
7	3,4,5-$(OCH_3)_3$	NA	0.00	0.43
8	2,3-$(OH)_2$	90.4±1.3 (7.95±0.34)	1.95	2.10
9	3-Cl	30.5±1.9	1.48	1.36
10	4-OCH_3	38.1±0.7	1.58	1.67
11	3-Br	29.9±1.0	1.48	1.38
12	styryl	31.7±0.2	1.50	1.47
13	4-*N*,*N*-$(CH_3)_2$	48.2±0.3	1.68	1.58
14	3,4-$(OH)_2$	81.7±1.0	1.91	1.89
15	2-OH-4-benzyloxy	2.4±1.4	0.38	0.36
16	3-OH	70.4±0.2	1.85	1.73
17	4-OH	66.1±0.2	1.82	1.89
18	3-OH-4-OCH_3	24.3±1.7	1.39	1.56
19	3,5-$(OH)_2$	74.0±0.2	1.87	1.75
20	2-OCH_3	85.4±0.2	1.93	1.97
21	H	39.0±0.9	1.59	1.74
22	2-OH-5-Cl	56.6±1.3	1.75	1.89
23	2-OH-5-NO_2	97.4±1.0 (0.9±0.01)	1.99	1.74
24	2-OH-3,5-$(Br)_2$	75.7±1.4	1.88	1.66
25	2,5-$(OH)_2$	90.8±1.2 (4.87±0.16)	1.96	2.08
26	4-Br	53.6±1.2	1.73	1.45
27	3-OCH_3-4-OH	41.6±0.8	1.62	1.74
28***	-	5.8±1.4	0.76	0.66

NA, no activity; *Data represent the average values of three determinations ± standard deviation; **Calculated by quantitative structure-activity relationship (QSAR) equation: log % hDPP III inh. = - 5.31 + 1.61 *IC1* + 0.79 *GATS6m* - 1.46 *EEig15d*; ***3-amino-2-methylquinazolin-4(3H)-one (precursor); numbers in brackets represent IC_{50} values in μM concentration.

Comparing the compounds that exhibited the strongest inhibition against the enzyme (Table 1), it is clear that they all have the OH group at position 2 of the phenyl ring. The importance of the OH group at position 2 of the phenyl ring for the inhibitory effect of the tested compounds can be concluded from the comparison of **3** and **23** having OH at position 2 (% inh. 90.3 and 97.4, respectively) with **21** without substituent on phenyl group (% inh. 39.0), and with **16** (% inh. 70.4) and **17** (% inh. 66.1) having the OH group at positions 3 and 4. In addition to OH at position 2, the presence of the nitro group at position 5 of the phenyl ring proved to be essential for **23** which exhibited the strongest inhibitory potential (% inh. 97.4) of all tested compounds. Compared to **3**, the additional OH group at positions 3, 4, or 5 of the phenyl ring in compounds **8**, **1**, and **25** had no effect on increasing the inhibitory potential toward the enzyme. However, compounds **14** (% inh. 81.7) and **19** (% inh. 73.9) with OH groups at positions 3 and 4 and positions 3 and 5, respectively, also show that the presence of OH groups is important for the inhibitory effect. It is evident that besides the OH group, the presence of a substituent such as chlorine or methoxy group at position 2 of the phenyl ring also contributes to the inhibitory potential, as shown by compounds **4**, **20**, and **6** (Table 1).

The addition of bromine at positions 3 and 5 in compound **24** and bromine or chlorine at position 5 in compounds **5** and **22**, respectively, causes a decrease in the inhibitory potential relative to compound **3**. Also, the addition of the ethoxy group at position 3 and the benzyloxy group at position 4 in compounds **2** and **15**, respectively, resulted in a reduction in their inhibitory effect on enzyme activity. The presence of bromine as the sole substituent on the phenyl ring showed a moderate inhibitory potential at position 4 in compound **26** (% inh. 53.6) and a mild inhibitory potential at position 3 in compound **11** (% inh. 29.9). Substitution of bromine with chlorine at position 3 did not affect inhibitory effect of compound **9**. Compound **10** having a methoxy group at position 3 showed slightly better inhibition (% inh. 38.1) compared to compound **18** (% inh. 23.4) with an additional OH group at position 2, however, switching positions of these two substituents in compound **27** caused increased enzyme inhibition (% inh. 41.6). Mild enzyme inhibition was shown in **13**, which had a dimethylamino group at position 4 of the phenyl ring, and **12** with a phenyl-allylidene group. Compound **28** used as a precursor for synthesis of the screened quinazolinone Schiff bases showed a weak inhibitory potential (% inh. 5.8) toward hDPP III.

3.2. QSAR analysis

The best multiple linear regression QSAR model (1) obtained for hDPP III inhibition is:

$$\log \%\ \text{hDPP III inh.} = -5.31 + 1.61\ IC1 + 0.79\ GATS6m - 1.46\ EEig15d \quad \text{Eq2}$$

where *IC1* is information content index (neighborhood symmetry of 1st order), *GATS6m* is a Geary autocorrelation of lag 6 weighted by mass, and *EEig15d* is the 15th eigenvalue from edge adjacency matrix weighted by dipole moment. The variables in equation are listed in order of their relative importance by the standardized regression coefficient.

Model satisfied the threshold values for fitting and internal validation criteria (Gramatica, 2007). The statistical parameters for obtained model are listed in Table 2. The values of the descriptors included in the model are given in the Supplementary Materials Table S1. The logarithmic values of hDPP III inhibition percentage, experimentally obtained and calculated by the model Eq2, are given in Table 1. Logarithmic values calculated by model equation that are slightly higher than 2 indicate that these compounds could be potent inhibitors at lower concentrations.

Table 2. The statistical parameters for the best QSAR model

Statistical Parameters	**Model 1**
N_{tr}	28
R^2	0.88
R^2_{adj}	0.87
s	0.18
F	59.16
K_{xx}	0.30
ΔK	0.11
$RMSE_{tr}$	0.16
MAE_{tr}	0.13
CCC_{tr}	0.94
Q^2_{LOO}	0.81
$RMSE_{cv}$	0.20
MAE_{cv}	0.16
CCC_{cv}	0.90
R^2_{Yscr}	0.11
Q^2_{Yscr}	-0.22
$RMSE_{AV\ Yscr}$	0.44
Applicability domain	
N outliers	1
N out of app. domain	-

LOO (leave-one-out); R^2 (coefficient of determination); R^2_{adj} (adjusted coefficient of determination); s (standard deviation of regression); F (Fisher ratio); K_{xx} (multivariate correlation index); ΔK (global correlation among descriptors); $RMSE_{tr}$ (root mean square error of the training set); MAE_{tr} (mean absolute error of the training set); CCC_{tr} (concordance correlation coefficient of the training set); Q^2_{LOO} (cross validated explained variance); $RMSE_{cv}$

(root mean square error of the training set determined through the cross validated method); MAE_{cv} (mean absolute error of the internal validation set); CCC_{cv} (concordance correlation coefficient test set using cross validation); R^2_{Yscr} (Y-scramble correlation coefficient); Q^2_{Yscr} (Y-scramble cross-validation coefficient); $RMSE_{AV\ Yscr}$ (root mean square error of Y randomization).

To exclude the possibility that the obtained model is overfitted, the collinearity of the descriptors has been evaluated with a correlation matrix (Table 3), which showed that all correlation coefficients *R* were lower than 0.7.

Table 3. Correlation matrix for the descriptors included in model 1

	IC1	***GATS6m***	***EEig15d***
IC1	1.00		
GATS6m	-0.41	1.00	
EEig15d	0.31	-0.16	1.00

Low collinearity between descriptors was also verified by the low value of K_{xx} and ΔK being higher than 0.05 (Todeschini et al., 1999). The model satisfied fitting criteria: both coefficient and adjusted coefficient of determination (R^2 and R^2_{adj}) are higher than 0.60; the concordance correlation coefficient of the training set (CCC_{tr}) is higher than 0.85; the root mean square error of the training set ($RMSE_{tr}$) and mean absolute error (MAE_{tr}) are close to zero (Table 2). Model also satisfied all of the following internal validation criteria (Gramatica, 2007): the cross-validated squared correlation coefficient Q^2_{LOO} needs to be higher than 0.6; the root mean square error determined through the cross-validated method ($RMSE_{cv}$) should be higher than the $RMSE_{tr}$; mean absolute error of the internal validation set (MAE_{cv}) close to zero. To check the robustness of the model and to eliminate chance correlation, Yrandomization test (Y-scrambling) was performed. Values of Y-scramble correlation coefficient (R^2_{Yscr}) and Y-scramble cross-validation coefficients (Q^2_{Yscr}) are both lower than 0.2 and R^2_{Yscr} is higher than Q^2_{Yscr}. Moreover, the root-mean-square error of Y-randomization ($RMSE_{AV\ Yscr}$) is higher than $RMSE_{cv}$, so the chance correlation of model was excluded (Kiralj & Ferreira, 2009). Williams plot revealed that there are no compounds outside of warning leverage ($h^* = 0.429$) but there is only one outlier, compound **7** (Figure 3).

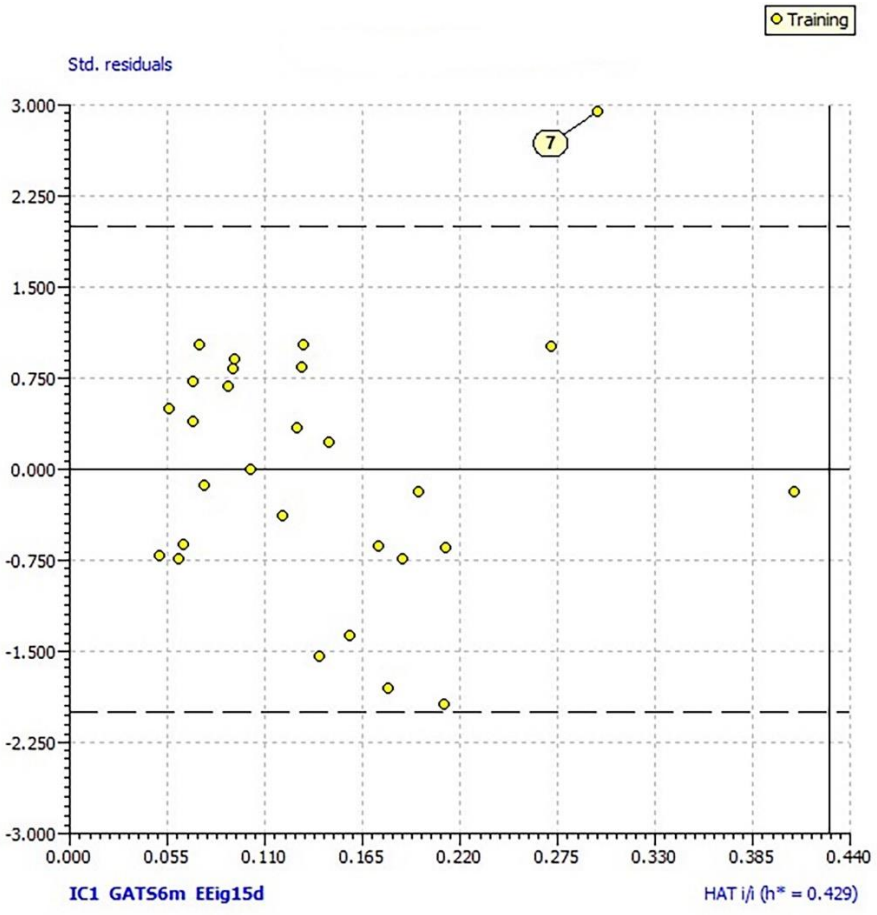

Figure 3. Williams plot (plot of standardized residuals vs. leverages (*h*) for each compound) of applicability domain of the Model 1. The warning leverage (*h**) is defined as $3p'/n$ (*n* is the number of training compounds, and *p'* the number of model adjustable parameters). Color figure can be viewed in the online issue.

The first descriptor in model equation, *IC1*, is an information content index, which describes neighborhood symmetry of 1st order. The information content descriptors evaluate and describe the effect of size, shape, and branching of molecules (Todeschini & Consonni, 2009). Therefore, a positive coefficient of *IC1* means that compounds with relatively higher values of this descriptor tended to exhibit higher inhibition of hDPP III. Since higher values of this descriptors mean more complex 1st order neighborhood, compounds with more diverse atom pairs may exhibit enhanced inhibition. The second descriptor, *GATS6m*, represents the Geary autocorrelation of lag 6 weighted by mass, and belongs to 2D autocorrelations. These descriptors reflect the contribution of pairs of atoms at the defined topological distance or spatial lag. The atoms represent the set of discrete points in space and the atomic property is the function evaluated at those points (Consonni & Todeschini, 2011). *GATS6m* describes dependence of one atom on value of mass of other atoms at the topological distance 6. Positive regression coefficient of this descriptor in model suggests a favorable effect of heavier atoms

at the 6 Å distance (Figure 4). The third descriptor in the equation is *EEig15d*, 15th eigenvalue from edge adjacency matrix, weighted by dipole moment. It belongs to the edge adjacency indices, derived from the edge adjacency matrix from a hydrogen-depleted molecular graph of molecules. Descriptor *EEig15d* is related to the molecular polarity, describing the distribution of electronic charge in molecule (Todeschini & Consonni, 2009; Estrada & Ramirez, 1996). Since the active compounds have negative values of this descriptor, and this descriptor has a negative regression coefficient in the model equation, it means that the presence of atoms higher polarity, such as oxygen atoms from hydroxyl groups, is related to the enhanced inhibition. The importance of hydroxyl groups has already been established in earlier studies (Agić et al., 2017; Agić et al., 2021).

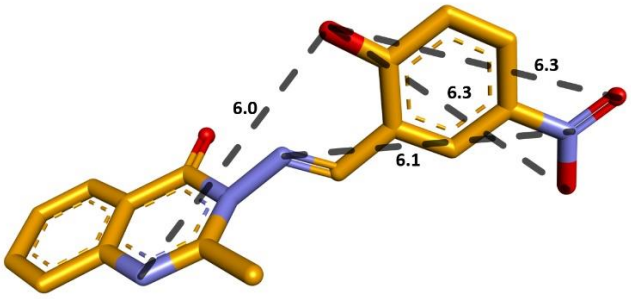

Figure 4. Interatomic distances in Å (colored black) of atom pairs shown on the optimized structure of the experimentaly most active compound (**23**). Color figure can be viewed in the online issue.

Although the obtained model is not predictive, it can provide some guidelines for the future compounds. According to the QSAR model, following structural features could improve the inhibition effect of quinazolinone Schiff bases against hDPP III:

a) substitution of hydrogen atoms from the quinazolinone core with various atomic groups that contribute to the molecular polarity (e.g., hydroxyl groups)

b) position these substituents at the 6 Å distance from the nitrogen and oxygen atoms of quinazolinone core.

The inspection of Williams plot (Figure 3) detected compound **7** as an outlier (compound with standardized residuals greater than 2 standard deviation units). The three methoxy groups of the phenyl ring decrease the overall neighborhood diversity and polarity of this compound. Also, these groups are sterically-crowded because of their vicinity, which is probably unfavorable for the hDPP III inhibition.

3.3. Molecular docking

The study was continued using molecular docking to obtain information on the possible mechanism of the five most active compounds (**1**, **3**, **8**, **23** and **25)** in terms of binding affinity and necessary intermolecular bonds formation responsible for observed enzyme inhibition. AutoDock Vina was used to find for the best pose of these compounds in the semi-closed form of hDPP III. The best pose predicted for compounds **23**, **8**, **25**, **1**, and **3** were located deep in the enzyme binding pocket near the lower β-sheet (residues 389–393) (Figure 5A) with docking scores of -8.9, -8.1, -8.0, -7.9, and -7.2 kcal mol^{-1}, respectively. The minimum distance between the catalytic Zn^{2+} ion and the screened compounds (C6 atom of the quinazolinone core) is ~ 4 Å and is less than the distance between the zinc cation and the nearest ligand atom (~ 7 Å) of docked inhibitor molecules 3-benzoyl-7-hydroxy-2H-chromen-2-one (Agić et al., 2021) and luteolin (Agić et al., 2017), suggesting that these compounds are positioned closer to the enzyme active site relative to these previously investigated inhibitors. Also, the position of the quinazolinone core of the docked compounds is close to the substrate position in the hDPP III active site (Tomić & Tomić, 2014; Zhang et al., 2021) which is accommodated similarly to the tynorphin in the peptide binding cleft (Bezerra et al, 2012).

According to the results given in Table 4 most compounds interact with a larger number of amino acids residues that are constituents of hDPP III S1 and S2 substrate binding subsites compared to the number of residues that are part of the S1', S2', and S3' subsites (Bezerra et al, 2012).

Table 4. Substrate binding subsites of hDPP III in complex with docked compounds. Subsites were defined according to Bezzera et al, 2012.

Residues	Subsites				
	S2	S1	S1'	S2'	S3'
PHE109	-	-	-	**25**	-
GLU316	**1, 3, 8, 23, 25**	-	-	-	-
TYR318	-	**1, 3, 8, 23, 25**	-	**1, 3, 8, 23, 25**	-
GLU329	-	**1, 3, 8, 23, 25**	-	-	-
PHE381	-	**1, 3, 8, 23**	-	-	-
PRO387	-	**1, 3, 8, 23, 25**	**1, 3, 8, 23, 25**	**1, 3, 8, 23, 25**	**1, 3, 8, 23, 25**
GLY389	-	**1, 3, 8, 23, 25**	**1, 3, 8, 23, 25**	-	-
ILE390	**1, 3, 8, 23, 25**	**1, 3, 8, 23, 25**	-	-	-
ASN391	**1, 3, 8, 23, 25**	-	-	-	-
GLU508	**1, 8, 23**	**1, 8, 23**	-	-	-
HIS568	**25**	**25**	**25**	-	-

Detailed analysis of the intermolecular bond formation for tested complexes obtained by Discovery studio software showed that the orientation of all docked compounds is conserved through interactions with the eleven identical hDPP III residues (Figure 5A). Most of these are van der Waals interactions between phenyl ring of the tested compounds and residues SER108, GLU316, SER317, ARG319, GLU327, and GLU329, as well as interactions between quinazolinone core and TYR318, PRO387, GLY389, ILE390, and ASN391 (Figure 5B-F).The exception is in the complex with compound **1,** where ARG319 formed hydrogen bond (H), GLU329 formed π-cation, and GLU387 and ILE390 formed π-alkyl interactions (Figure 5B right); compound **3** where GLU316, ARG319 and PRO387 formed H bond, pi-donor H bond, and π-alkyl interaction, respectively (Figure 5C right); compound **8** where GLU329 formed H bond while PRO387 and ILE390 formed π-alkyl interactions (Figure 5D right); compound **23** where SER317, TYR318 and GLU329 formed H bonds, and PRO387 and ILE390 with π-alkyl interactions (Figure 5E right); compound **25** where GLU327 formed H bond (Figure 5F right). In addition to the latter eleven residues, conformational stability of **1**, **8**, and **23** were associated with six binding residues, while in **3** and **25** with three and four residues, respectively (Figure 5B-F left). Among them, notable are van der Waals interactions of important catalytic residues: HIS568 with compound **25** and GLU451 with **1**, **8**, and **23**. The results of the above analysis of intermolecular bond are in accordance with the part of discussion in Chapter 3.1., that the presence of the OH group at position 2 of the phenyl ring of the tested compounds has the effect of increasing their inhibitory potential. Indeed, this OH group in all five most active compounds participates in hydrogen bonding with hDPP III residues as illustrated in Figure 5B-F right.

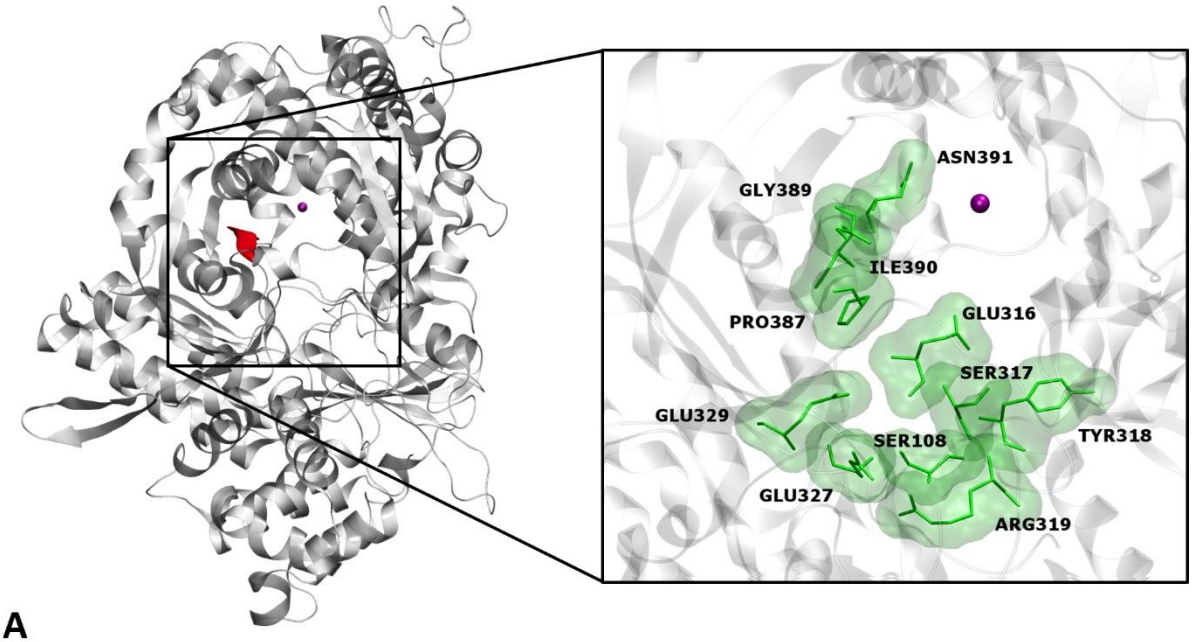
ASN391
GLY389
ILE390
PRO387
GLU316
SER317
GLU329
SER108
TYR318
GLU327
ARG319

A

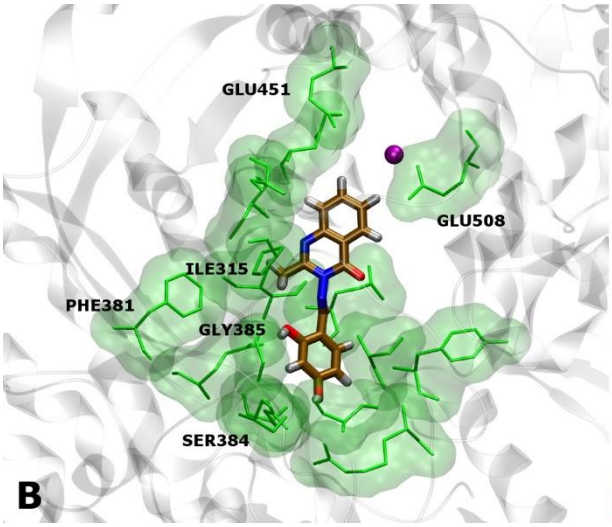
GLU451
GLU508
ILE315
PHE381
GLY385
SER384

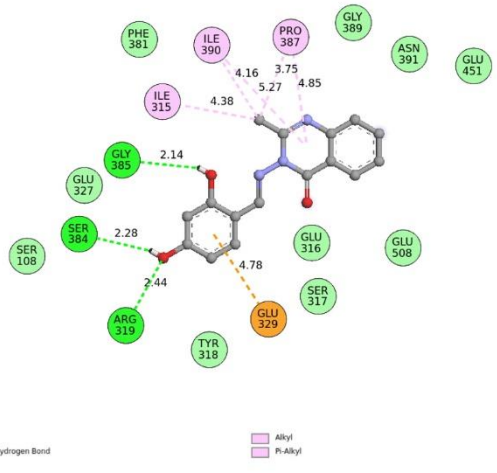
PHE 381
ILE 390
PRO 387
GLY 389
ASN 391
GLU 451
4.16
3.75
5.27
4.85
ILE 315
4.38
GLY 385
2.14
GLU 327
SER 384
2.28
SER 108
GLU 316
GLU 508
4.78
2.44
SER 317
ARG 319
GLU 329
TYR 318
Interactions
van der Waals
Conventional Hydrogen Bond
Pi-Anion
Alkyl
Pi-Alkyl

B

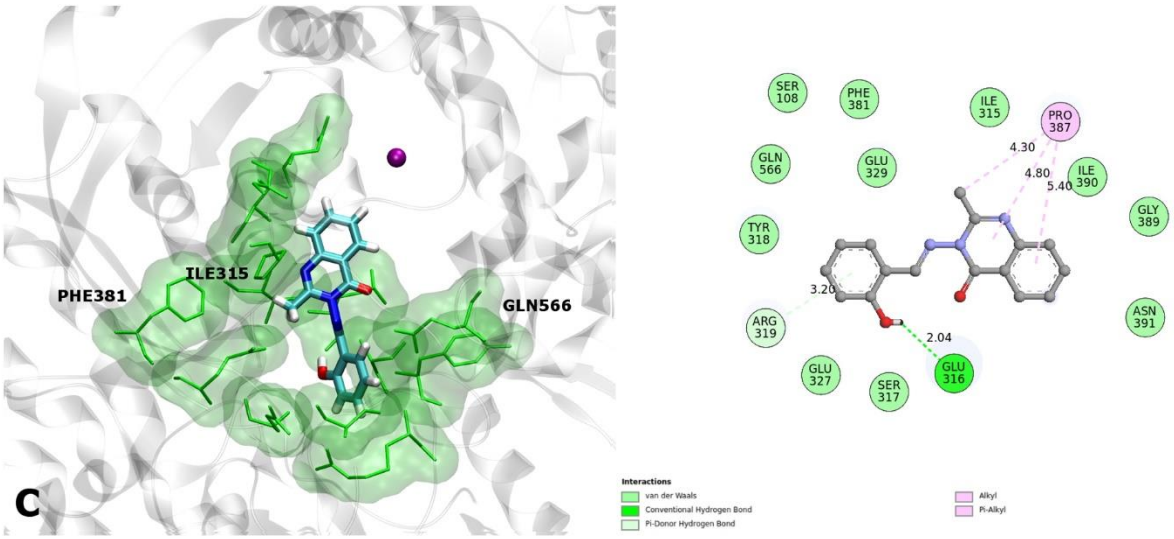
ILE315
PHE381
GLN566
C
SER 108
PHE 381
ILE 315
PRO 387
GLN 566
GLU 329
ILE 390
GLY 389
TYR 318
4.30
4.80
5.40
3.20
ARG 319
ASN 391
2.04
GLU 327
SER 317
GLU 316
Interactions
van der Waals
Conventional Hydrogen Bond
Pi-Donor Hydrogen Bond
Alkyl
Pi-Alkyl

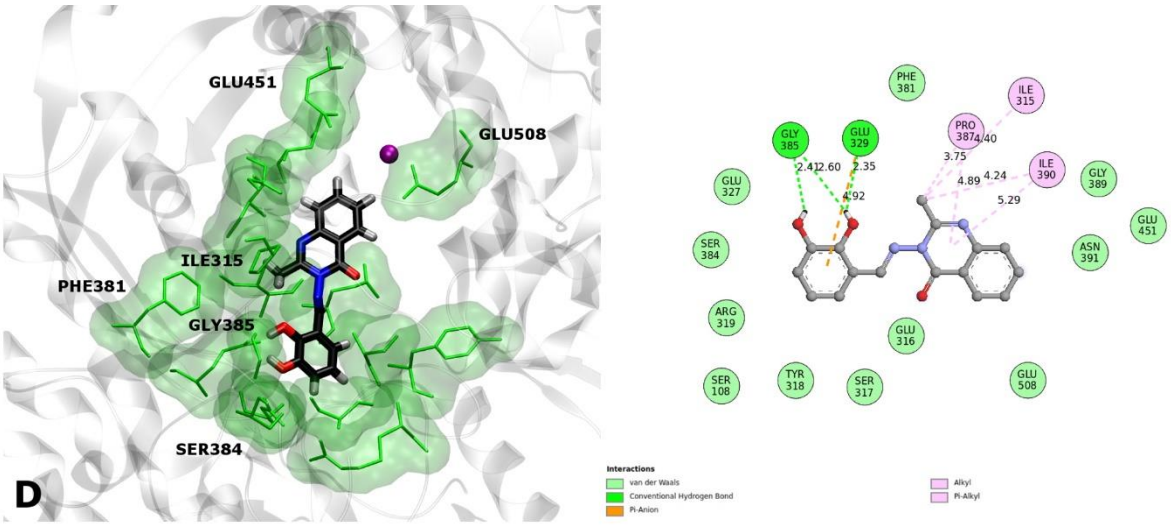
GLU451
GLU508
ILE315
PHE381
GLY385
SER384
D
PHE 381
ILE 315
GLY 385
GLU 329
PRO 387
3.75
4.40
2.41
2.60
2.35
ILE 390
GLY 389
GLU 327
4.89
4.24
4.92
5.29
GLU 451
SER 384
ASN 391
ARG 319
GLU 316
SER 108
TYR 318
SER 317
GLU 508
Interactions
van der Waals
Conventional Hydrogen Bond
Pi-Anion
Alkyl
Pi-Alkyl

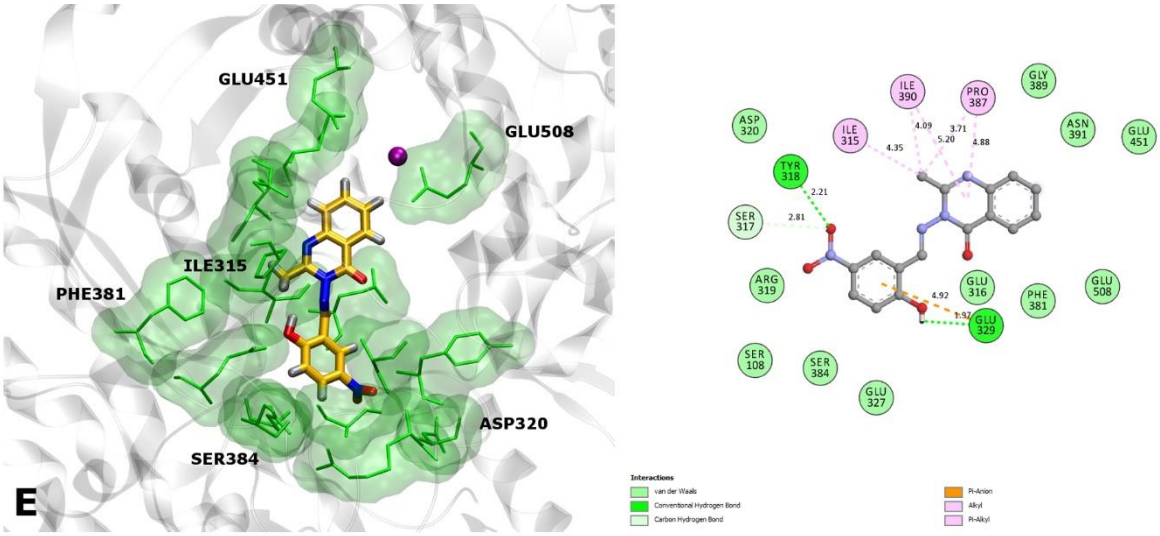
GLU451
GLU508
ILE315
PHE381
ASP320
SER384
E
ILE 390
PRO 387
GLY 389
ASP 320
ILE 315
4.09
3.71
ASN 391
GLU 451
5.20
4.88
4.35
TYR 318
2.21
SER 317
2.81
ARG 319
GLU 316
PHE 381
GLU 508
4.92
1.97
GLU 329
SER 108
SER 384
GLU 327
Interactions
van der Waals
Conventional Hydrogen Bond
Carbon Hydrogen Bond
Pi-Anion
Alkyl
Pi-Alkyl

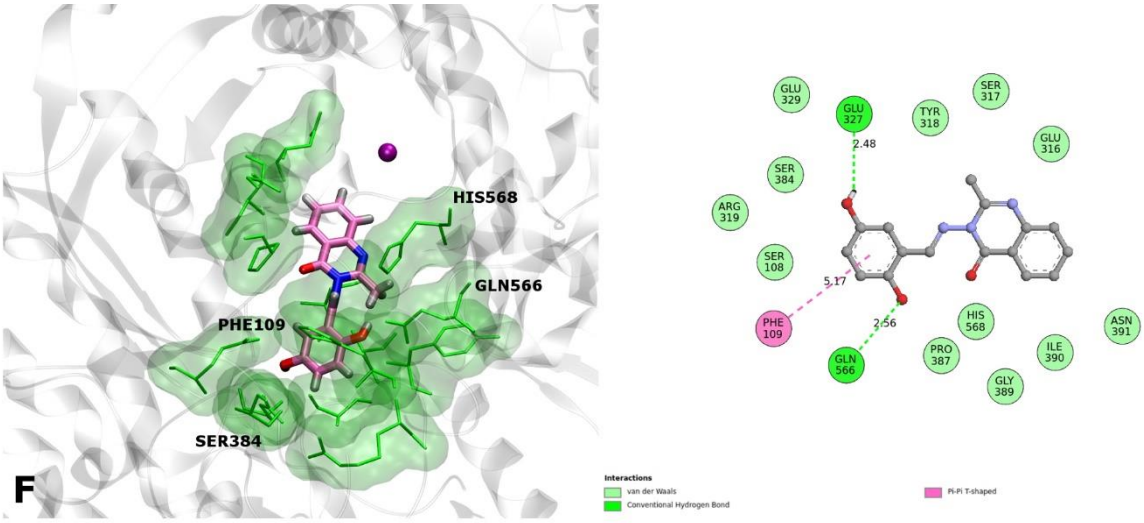

Figure 5. Docked pose of the five most active compounds at the hDPP III binding site. **A** Surface representation of the protein showing the binding site of the same enzyme residues involved in the interactions with all docked compounds. The lower β sheet is colored in red, and zinc cation is represented as a purple sphere. **B-F** (Left) 3D representations of the rest of the interacting enzyme residues, not listed on **A** (for clarity), and 2D diagram (right) of all enzyme interactions with compounds **1 (B)**, **3 (C)**, **8 (D)**, **23 (E)** and **25 (F)**, colored brown, cyan, black, orange and pink, respectively. Color figure can be viewed in the online issue.

3.4. MD simulations

It is well known that molecular dynamics (MD) simulation provide powerful tools to study the dynamic molecular mechanisms of ligand (inhibitor) - receptor (enzyme) complexes (Chen et al., 2020; Shi et al., 2020). Therefore, MD simulations were carried out on the best docked pose of the most potent inhibitor (compound **23**) in complex with semi-closed form of hDPP III to further explore the ligand-receptor interactions. Productive 210 ns-long MD simulation of the complex was performed using the programme package AMBER16, and intermolecular interactions, including native contacts and hydrogen bonding were analysed throughout. Root mean square deviation (RMSD) was used to analyse dynamic behaviour and protein stability during simulation. The optimised structure of the complex was used to describe types of interactions in more detail.

3.4.1. RMSD of the protein backbone atoms

Figure 6 presents an analysis for the RMSD as a function of simulation time of the protein backbone atoms for free hDPP III and in complex with **23**. According to the RMSD profiles, the complexed protein fluctuates less in the first 100 ns of MD simulations compared to the free protein. The average RMSD value calculated during the whole simulation time for complex and free enzyme is 1.43±0.17 Å and 1.61±0.22 Å, respectively. Stabilization of

complexed protein is slightly better from the 60th to the 100th ns (average RMSD±SD 1.39±0.08 Å) and in the last 50 ns of MD simulations (average RMSD±SD 1.57±0.09 Å).

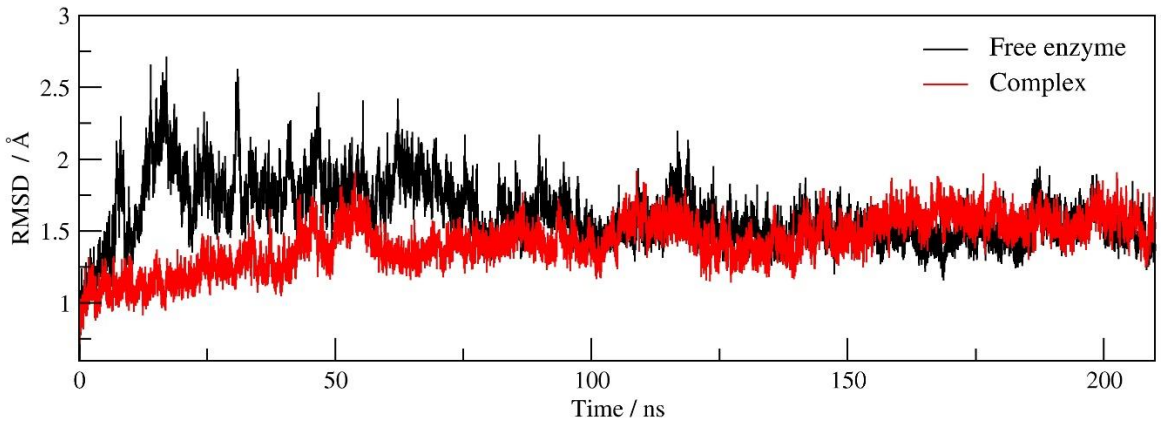

Figure 6. RMSD of the hDPP III backbone atoms obtained during 210 ns of MD simulation. Color figure can be viewed in the online issue.

3.4.2. Native Contacts

Furthermore, we studied the interactions between receptor (protein) and ligand (compound **23**) by calculating the relative occupancy of native contacts during the simulation time. The relative occupancy of native contacts is the sum of fractions of native contacts during the entire trajectory for each residue pair relative to the total number of native contacts involved with that pair. Native contacts were defined as a distance between the atoms of receptor residues and ligand atoms within a distance cutoff of 5 Å. The *nativecontacts* command in the CPPTRAJ module was used to calculate fractions of native contacts during simulations.

Figure 7 and Figure S1 illustrates the protein residues that were involved in forming of native contacts with relative occupancy above 50% during last 110 ns of simulation time, i.e. after system stabilization. Most native contacts (11) are formed with relative occupancy from 50% to 80% while the remaining three are involved in forming native contacts with relative occupancy >80%. Quinazolinone core of **23** mostly forms native contacts in the hydrophobic region of the interdomain binding cleft with PHE109, ILE386, PRO387, and HIS568, while phenyl ring forms native contacts in the weak hydrophobic region comprised by residues SER314, GLU316, SER317, TYR318, ARG319, GLY326, GLU327, GLU329, SER384 and GLY385.

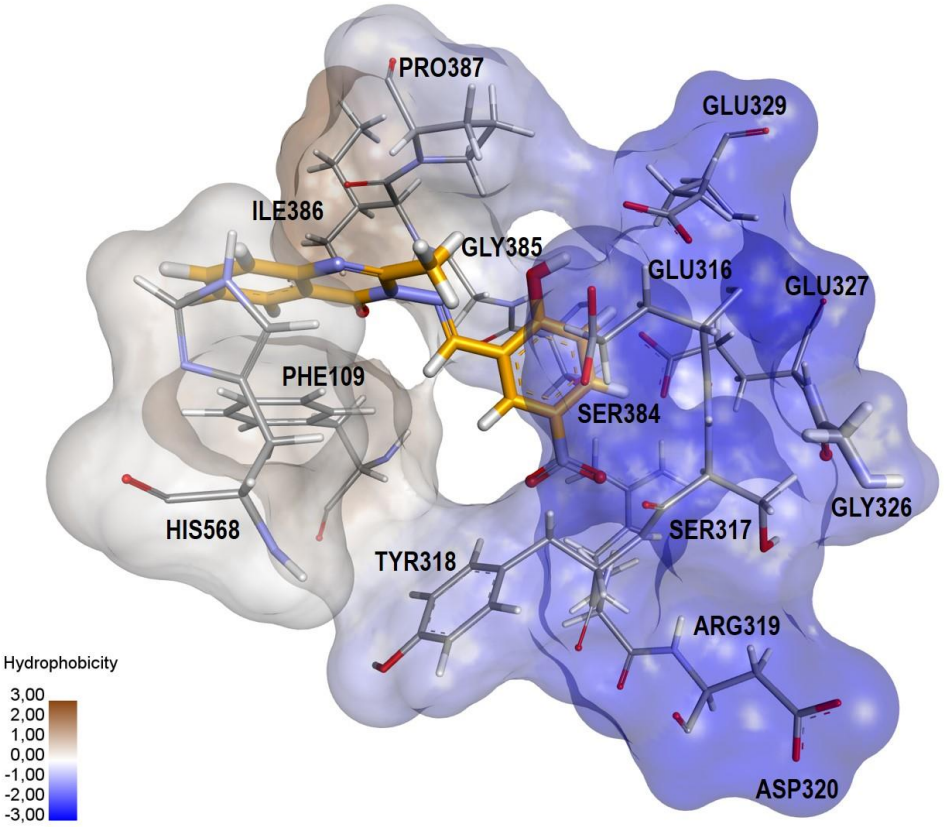

Figure 7. Hydrophobic surfaces of protein residues involved in native contacts formation with **23** (orange) during last 110 ns of MD simulations. The amino acid interacting residues are shown in stick representation. Color figure can be viewed in the online issue.

Long MD simulations of hDPP III in complex with synthetic inhibitors, such as guanidinocarbonylpyrrole conjugates (Matić et al., 2016; Ćehić et al., 2020) or coumarin derivatives (Agić et al., 2021) have shown the active participation of some of these residues (e.g., GLU316, TYR318 and PHE109) in stabilization of compounds during their binding to the enzyme active site. By comparing amino acid residues that form native contacts in the complex with compound **23** (Figure 7) with the enzyme residues that form intermolecular bonds in the best docked pose of **23** (Figure 5E), it can be seen that the largest number of identical residues (GLU316, SER317, TYR318, ARG319, ASP320, GLU327, GLU329, and SER384) converged with the phenyl ring and only one residue (PRO387) with the quinazolinone core of compound **23**. The reason for the weak convergence of protein residues and the quinazolinone core obtained by molecular docking and MD simulations is the movement of the quinazolinone core during system equilibration. Namely, in the first step of equilibration, the quinazolinone core of compound **23** moves from its starting position, and in the second step, it assumes an orientation that remains preserved until the system stabilization (Figure S2) and throughout the remaining time of the MD simulation (Figure 8). Of the 14 residues mentioned above that form

native contacts with compound **23**, seven of them (PRO387, GLU316, SER317, TYR318, ARG319, GLU327, and GLU329) form intermolecular bonds with all other tested compounds (Figure 5A-F). A possible explanation for the differences in IC_{50} observed between compounds with lower IC_{50} and compounds **1**, **3** and **8** is an additional intermolecular bond of compounds **23** and **25** with PHE109, which was subsequently shown to be relevant protein residue involved in native contact formation with **23**.

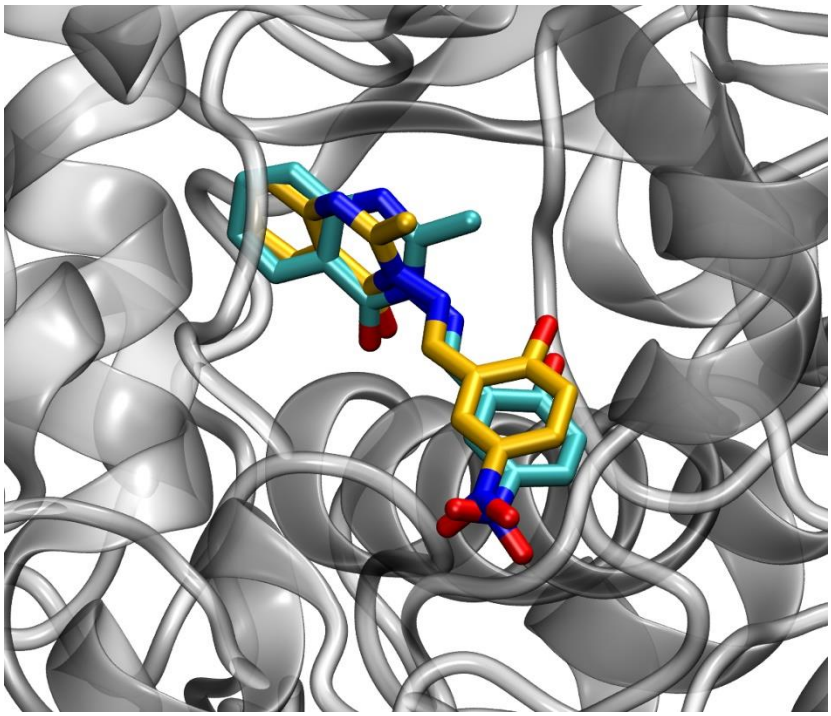

Figure 8. Overlay of the hDPP III-compound **23** complexes obtained after 110 ns (cyan) and 210 ns (orange). Color figure can be viewed in the online issue.

3.4.3. Types of intermolecular interactions

To perform a detailed analysis of different types of intermolecular interactions, the extracted structure of hDPP III in complex with **23** obtained from the trajectory after 210 ns of MD simulations was optimized and used as a representative. As can be seen from Figure 9 and Figure S2, more interactions are formed between the phenyl ring of compound **23** and hDPP III residues relative to the quinazolinone core. The phenyl ring of **23** formed van der Waals interactions with GLU316, SER317, GLU327, and SER384 whereas the quinazolinone core formed this type of interaction only with MET569. Furthermore, the methyl group of the

quinazolinone core forms an alkyl bond with PRO387, while the core itself forms three π-type interactions (Figure S3). The interplanar distances and angles between quinazolinone core of **23** and the phenyl ring of PHE109, imidazole ring of HIS568 as well as distances and angle between quinazolinone core of **23** and the amide group of ILE386 (measured between intermolecular atoms as shown in Figures S4, S5 and S6, respectively) indicate π-π stacking, π-π T-shape and amide-π stacking interactions in the most time of MD simulations. According to the 2D depiction in Figure S2 the OH group at position 2 of the phenyl ring of compound **23** forms an H-bond with GLU329, the oxygen atom of the quinazolinone core forms an H-bond with ILE386, and oxygen from the nitro group forms H bonds with TYR318 and ARG319. Additionally, another oxygen atom of the nitro group forms a carbon-H bond with SER108.

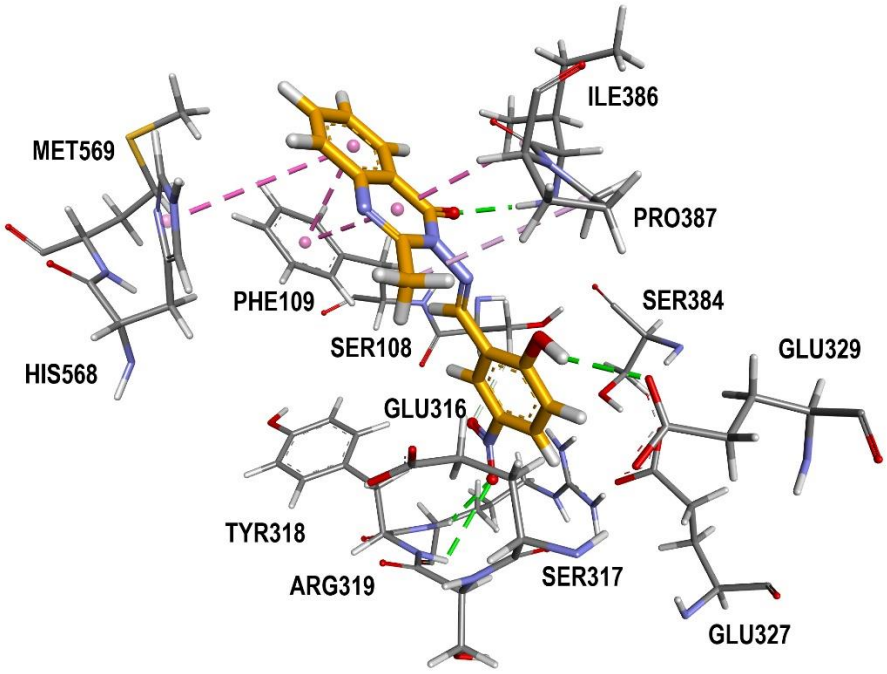

Figure 9. 3D interactions of compound **23** with amino acid residues of hDPP III obtained after 210 ns of MD simulations as presented in the 2D scheme (Figure S2). Color figure can be viewed in the online issue.

The results of trajectory H-bonds analysis calculated by *hbond* command in CPPTRAJ module showed there were four H-bonds formed during the MD process with the occupation time >10% (Table S2 and Figure 10). After system stabilisation (last 110 ns of the simulation time) the first H-bond is formed by the OE2 atom of GLU329 and hydroxyl group on the phenyl ring of compound **23** (Figure 10 A) with an occupation time of 83%. The second and third H-bond was formed between the H-N of ARG319 and the O2 and O3 atoms of the nitro group of **23** with the occupation time of 11 % and 12 %, respectively (Figure 10 C and D). These results

are in accordance with the experimental analyses which have shown that the presence of the OH group at position 2 and the nitro group at position 5 of the phenyl ring is crucial to achieving a substantial inhibitory potential of the test compounds. Only one H bond with the occupation time of 68% was formed during the simulations by the carbonyl oxygen of the quinazolinone core and H-N of ILE386 (Figure 10 B). The involvement of GLU329 has been reported in the formation of a H-bond with the OH group at C7 of coumarin derivative (Agić et al., 2021) suggesting that this residue as well as the carbonyl oxygen and OH group plays an important role in stabilizing quinazolinone core and the phenyl ring of **23** in their binding to hDPP III.

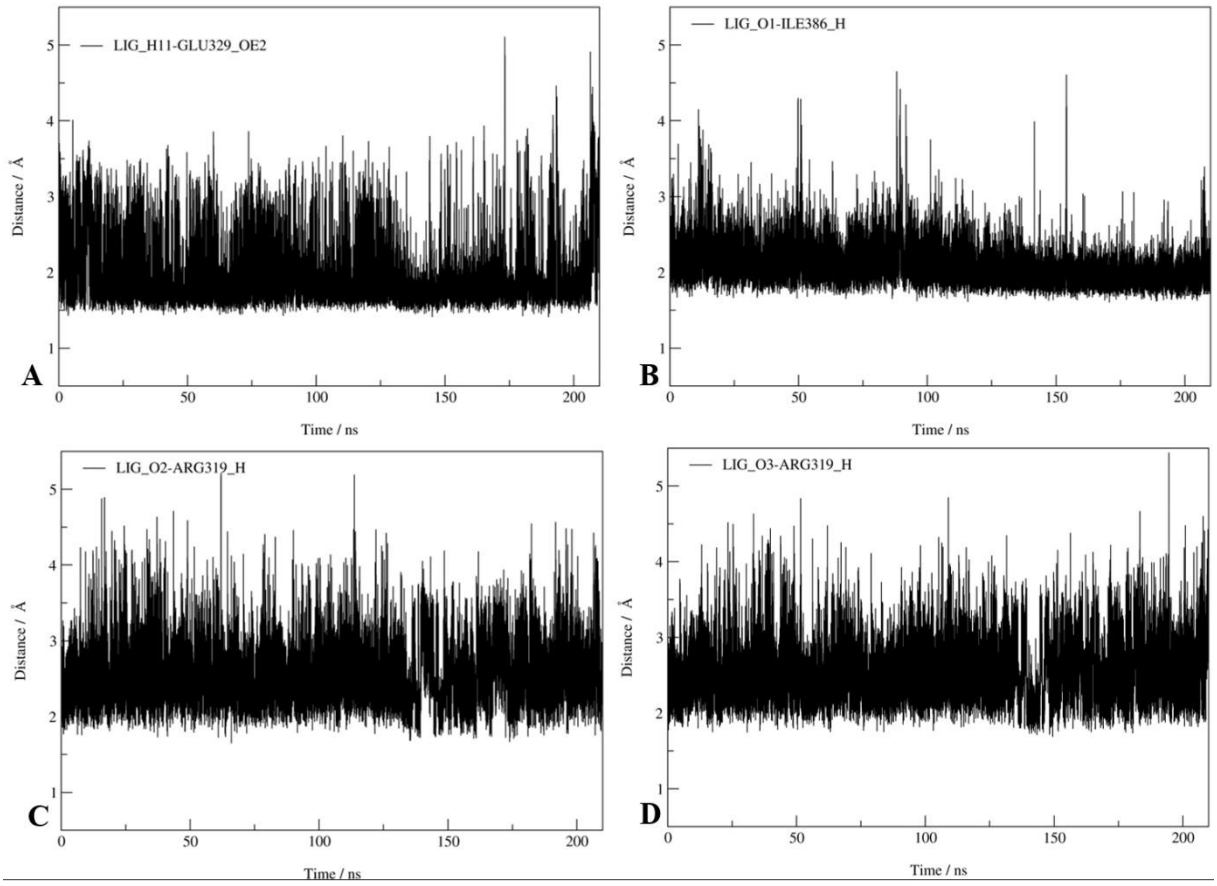

Figure 10. Formation of the hydrogen bonds between compound **23** (LIG) and GLU329, ILE386 and ARG319 during 210 ns of MD simulations.

4. Conclusions

In this paper, we report for the first time the inhibition profiles of quinazolinone-Schiff's bases against the hDPP III combining an *in vitro* experiment with an *in silico* molecular modeling study. Most of the 28 tested compounds exhibited inhibitory activity at the 100 μM concentration. QSAR revealed that the higher diversity of neighboring atom pairs, distribution

of heavier atoms at the 6 Å distance from each other, and the presence of higher polarity atoms contribute to the enhanced enzyme inhibition. The best docking pose predicts that the five most active compounds bind to the interdomain cleft, near the enzyme active site, while molecular dynamics simulations of the best inhibitor **23** (IC_{50}=0.96 μM) indicate that the hydroxyl group on phenyl ring and carbonyl group on quinazolinone core of **23**, as well as interactions with GLU329 and ILE386, PHE109, ARG319, and GLU327 are important for the inhibitor binding and stabilization to the hDPP III active site.

Acknowledgments:

This work has been supported by the Croatian Science Foundation under the projects IP-2018-01-2936, UIP-2017-05-6593 and the Isabella cluster (http://www.srce.unizg.hr/en/isabella/).

References

Abramić, M.; Zubanović, M.; Vitale, L. Dipeptidyl peptidase III from human erythrocytes. *Biol. Chem. Hoppe-Seyler*. **1988**, *369*, 29–38. doi: 10.1515/bchm3.1988.369.1.29

Agić, D.; Brkić, H.; Tomić, S.; Karačić, Z.; Špoljarević, M.; Lisjak, M.; Bešlo, D.; Abramić, M. Validation of flavonoids as potential dipeptidyl peptidase III inhibitors: Experimental and computational approach. *Chem. Biol. Drug Des.* **2017**, *89*, 619-627. https://doi.org/10.1111/cbdd.12887

Agić, D.; Karnaš, M.; Šubarić, D.; Lončarić, M.; Tomić, S.; Karačić, Z.; Bešlo, D.; Rastija, V.; Molnar, M.; Popović, B. M.; Lisjak, M. Coumarin derivatives act as novel inhibitors of human dipeptidyl peptidase III: Combined in vitro and in silico study. *Pharmaceuticals*. **2021**,14 (6), 540. https://doi.org/10.3390/ph14060540

Baršun, M.; Jajčanin, N.; Vukelić, B.; Špoljarić, J.; Abramić, M. Human dipeptidyl peptidase III acts as a post-proline-cleaving enzyme on endomorphins. *Biol. Chem.* **2007**, *388*, 343–348. doi: 10.1515/BC.2007.039

Bezerra, G. A.; Dobrovetsky, E.; Viertlmayr, R.; Dong, A.; Binter, A.; Abramić, M.; Macheroux, P.; Dhe-Paganon, S.; Gruber, K. Entropy-driven binding of opioid peptides induces a large domain motion in human dipeptidyl peptidase III. *Proc. Natl. Acad. Sci. U.S.A.* **2012**, *109*, 6525–6530. doi: 10.1073/pnas.1118005109

Blagojević, B.; Agić, D.; Serra, A. T.; Matić, S.; Matovina, M.; Bijelić, S.; Popović, B. M. An in vitro and in silico evaluation of bioactive potential of cornelian cherry (*Cornus mas* L.) extracts rich in polyphenols and iridoids. *Food Chem.* **2021**, *335*, 127619.https://doi.org/10.1016/j.foodchem.2020.127619

Case, D.; Betz, R.; Cerutti, D.; Cheatham, T.E. III.; Darden, T.; Duke, R. E.; Giese, T.; Gohlke, H.; Goetz, A. W.; Homeyer, N.; et al. AMBER 2016. **2016**, University of California, San Francisco.

Ćehić, M.; Sućˇ Sajko, J.; Karačić, Z.; Piotrowski, P.; Šmidlehner, T.; Jerić, I.; Schmuck, C.; Piantanida, I.; Tomić, S. The guanidiniocarbonylpyrrole-fluorophore conjugates as theragnostic tools for dipeptidyl peptidase III monitoring and inhibition. *J. Biomol. Struct. Dyn.* **2020**, *38*, 3790-3800. https://doi.org/10.1080/07391102.2019.1664936

Chen, J. M.; Barrett, A. J. Dipeptidyl-peptidase III. In *Handbook of Proteolytic Enzymes*, 2nd ed.; Barrett A. J., Rawlings N. D., Woessner J. F. (Eds.),; Elsevier Academic Press: Amsterdam, 2004; Vol. 1, pp. 809–812.

Chen, J.; Liu, X.; Zhang, S.; Chen, J.; Sun, H.; Zhang, L.; Zhang, Q. Molecular mechanism with regard to the binding selectivity of inhibitors toward FABP5 and FABP7 explored by multiple short molecular dynamics simulations and free energy analyses. Phys. Chem. Chem. Phys. 2020, 22, 2262-2275. doi: 10.1039/c9cp05704h

Consonni, V.; Todeschini, R. Structure-Activity Relationships by Autocorrelation Descriptors and Genetic Algorithms. In Chemoinformatics and Advanced Machine Learning Perspectives: Complex Computational Methods and Collaborative Techniques. Lodhi, H; Yamanishi Y. Eds., IGI Global: Hershey, USA, 2011, pp 60-94. 10.4018/978-1-61520-911-8.ch005

Dassault Systèmes BIOVIA. *Discovery Studio Visualizer, Release 2019.* Dassault Systèmes; San Diego, CA, USA: **2019**.

Eriksson, L.; Jaworska, J.; Worth, A.P.; Cronin, M.T.D.; McDowell, R.M.; Gramatica, P. Methods for reliability and uncertainty assessment and for applicability evaluations of classification- and regression-based QSARs. *Environ. Health Perspect.* **2003**, 111, 1361-1375. https://doi.org/10.1289/ehp.5758

Estrada E.; Ramirez A. Edge Adjacency Relationships and Molecular Topographic Descriptors. Definition and QSAR Applications. *J. Chem. Inf. Comput. Sci.* **1996**, *36*, 837-843. https://doi.org/10.1021/ci950186z

Gramatica, P. Principles of QSAR models validation: Internal and external. *QSAR. Comb. Sci.* **2007**, *26*, 694-701. http://dx.doi.org/10.1002/qsar.200610151

Gramatica, P.; Chirico, N.; Papa, E.; Cassani, S.; Kovarich, S. QSARINS: A new software for the development,analysis, and validation of QSAR MLR models. *J. Comput. Chem.* **2013**, 34, 2121-2132. https://doi.org/10.1002/jcc.23361

GraphPad Prism version 5.0.0 for Windows, GraphPad Software, San Diego, California USA, www.graphpad.com

Hanwell, M.D.; Curtis, D.E.; Lonie, D.C.; Vandermeersch, T.; Zurek, E.; Hutchison, G.R. Avogadro: an advanced semantic chemical editor, visualization, and analysis platform. *J. Cheminform.* **2012**, 4, 17. https://doi.org/10.1186/1758-2946-4-17

Harney, A.S.; Sole, L.B.; Meade, T.J. Kinetics and thermodynamics of irreversible inhibition of matrix metalloproteinase 2 by a Co(III) Schiff base complex. *J. Biol. Inorg. Chem.* **2012**, 17, 853-860. https://doi.org/10.1007/s00775-012-0902-3

He, M.; Mangiameli, D.P.; Kachala, S.; Hunter, K.; Gillespie, J.; Bian, X.; Shen, H.-C.J.; Libutti, S.K. Expression signature developed from a complex series of mouse models accurately predicts human breast cancer survival. *Clin. Cancer Res.* **2010**,16, 249-259. doi: 10.1158/1078-0432.CCR-09-1602

Hocquet, A.; Langgård, M. An Evaluation of the MM+ Force Field. *J. Mol. Model.* **1998**, 4, 94-112. https://doi.org/10.1007/s008940050128

Hricovíniová, Z.; Hricovíni, M.; Kozics, K. New series of quinazolinone derived Schiff's bases: synthesis, spectroscopic properties and evaluation of their antioxidant and cytotoxic activity. *Chem. Pap.* **2018**, 72, 1041-1053. https://doi.org/10.1007/s11696-017-0345-y

Humphrey, W.; Dalke, A.; Schulten, K. VMD-visual molecular dynamics. *J. Mol. Graph.* **1996,** *14*, 33–38. https://doi.org/10.1016/0263-7855(96)00018-5.

Jha, S.; Taschler, U.; Domenig, O.; Poglitsch, M.; Bourgeois, B.; Pollheimer, M.; Pusch, L. M.; Malovan, G.; Frank, S.; Madl, T.; et al. Dipeptidyl peptidase 3 modulates the renin-angiotensin system in mice. *J. Biol. Chem.* **2020**, *295*, 13711–13723. https://doi.org/10.1074/jbc.RA120.014183

Kajal, A.; Bala, S.; Kamboj, S.; Sharma, N.; Saini, V. Schiff Bases: A Versatile Pharmacophore. *Journal of Catalysts*. **2013**, 2013, ID 893512. https://doi.org/10.1155/2013/893512

Karačić, Z.; Špoljarić, J.; Rožman, M.; Abramić, M. Molecular determinants of human dipeptidyl peptidase sensitivity to thiol modifying reagents. *Biol. Chem.* **2012**, *393*, 1523–1532. doi: 10.1515/hsz-2012-0181

Kiralj, R.; Ferreira, M.M.C. Basic validation procedures for regression models in QSAR and QSPR studies: Theory and application. *J. Braz. Chem. Soc.* **2009**, 20, 770-787. doi:10.1590/S0103-50532009000400021

Komar, M.; Prašnikar, F.; Gazivoda Kraljević, T.; Aladić, K.; Molnar, M. 3-Amino-2-methylquinazolin-4-(3H)-one Schiff Bases Synthesis - A Green Chemistry Approach - A Comparison of Microwave and Ultrasound Promoted Synthesis with Mechanosynthesis. *Curr. Green Chem.* **2021**, 8(1), 62-69. doi:10.2174/2213346107999201231125434

Kumar, P.; Reithofer, V.; Reisinger, M.; Wallner, S.; Pavkov-Keller, T.; Macheroux, P.; Gruber, K. Substrate complexes of human dipeptidyl peptidase III reveal the mechanism of enzyme inhibition. *Sci. Rep.* **2016**, *6*, 23787. doi: 10.1038/srep23787

Li, J.J.; Nahra, J.; Johnson, A.R.; Bunker, A.; O'Brien, P.; Yue, W.S.; Ortwine, D.F.; Man, C.F.; Baragi, V.; Kilgore, K. et al. Quinazolinones and pyrido[3,4-d]pyrimidin-4-ones as orally active and specific matrix metalloproteinase-13 inhibitors for the treatment of osteoarthritis. *J. Med. Chem.* **2008**, 51(4), 835-841. doi: 10.1021/jm701274v

Liu, Y.; Kern, J. T.; Walker, J. R.; Johnson, J. A.; Schultz, P. G.; Luesch, H. A genomic screen for activators of the antioxidant response element. *Proc. Natl. Acad. Sci. U.S.A.* **2007**, *104*, 5205-5210. https://doi.org/10.1073/pnas.0700898104

Lu, K.; Alcivar, A. L.; Ma, J.; Foo, T. K.; Zywea, S.; Mahdi, A.; Huo, Y.; Kensler, T. W.; Gatza, M. L.; Xia, B. NRF2 induction supporting breast cancer cell survival is enabled by oxidative stress–induced DPP3–KEAP1 interaction. *Cancer Res*. **2017**, 77, 2881-2892. doi: 10.1158/0008-5472.CAN-16-2204

Maier, J. A.; Martinez, C.; Kasavajhala, K.; Wickstrom, L.; Hauser, K. E.; Simmerling, C. ff14SB: Improving the Accuracy of Protein Side Chain and Backbone Parameters from ff99SB. *J. Chem. Theory Comput.* **2015**, *11*, 3696-3713. https://doi.org/10.1021/acs.jctc.5b00255

Matić, J.; Šupljika, F.; Tir, N.; Piotrowski, P.; Schmuck, C.; Abramić, M.; Piantanida, I.; Tomić, S. Guanidiniocarbonyl-pyrrole-aryl conjugates as inhibitors of human dipeptidyl peptidase III: combined experimental and computational study. *RSC Adv.* **2016**, *6*, 83044–83052. https://doi.org/10.1039/C6RA16966J

Matić, S.; Kekez, I.; Tomin, M.; Bogár, F.; Šupljika, F.; Kazazić, S.; Hanić, M.; Jha, S.; Brkić, H.; Bourgeois, B.; et al. Binding of dipeptidyl peptidase III to the oxidative stress cell sensor Kelch-like ECH-associated protein 1 is a two-step process. *J. Biomol. Struct. Dyn.* **2020**, 1-12. doi: 10.1080/07391102.2020.1804455

Pang, X.; Shimizu, A.; Kurita, S.; Zankov, D.P.; Takeuchi, K.; Yasuda-Yamahara, M.; Kume. S.; Ishida, T.; Ogita, H. Novel therapeutic role for dipeptidyl peptidase III in the treatment of hypertension. *Hypertension.* **2016**, *68*, 630–641. https://doi.org/10.1161/HYPERTENSIONAHA.116.07357

Prajapati, S.C.; Chauhan, S. S. Human dipeptidyl peptidase III mRNA variant I and II are expressed concurrently in multiple tumor derived cell lines and translated at comparable efficiency in vitro. *Mol. Biol. Rep*. **2016**, 43, 457-462. doi.org/10.1007/s11033-016-3996-9

Radwan, A.A.; Alanazi, F.K. Biological Activity of Quinazolinones. In Quinazolinone and Quinazoline Derivatives, Al-kaf A.G. Eds., IntechOpen: London. UK, 2020. 10.5772/intechopen.90621.

Rakesh, K.P.; Manukumar, H.M.; Channe Gowda, D. Schiff's bases of quinazolinone derivatives: Synthesis and SAR studies of a novel series of potential anti-inflammatory and antioxidants, *Bioorg. Med. Chem. Lett.* **2015**, 25 (5), 1072-1077. https://doi.org/10.1016/j.bmcl.2015.01.010

Ryckaert, J. P.; Ciccotti, G.; Berendsen, H. J.C. Numerical Integration of the Cartesian Equations of Motion of a System with Constraints: Molecular Dynamics of n-Alkanes. *J. Comput. Phys.* **1977**, *23*, 327–341. https://doi.org/10.1016/0021-9991(77)90098-5.

Sato, H.; Kimura, K.; Yamamoto, Y. Hazato, T. Activity of DPP III in human cerebrospinal fluid derived from patients with pain. *Masui.* **2003**, *52*, 257-263.

Shi, N.; Zheng, Q.; Zhang, H. Molecular Dynamics Investigations of Binding Mechanism for Triazoles Inhibitors to CYP51. Front. Mol. Biosci. 2020, 7, 586540. doi: 10.3389/fmolb.2020.586540.

Šimaga, Š.; Babić, D.; Osmak, M.; Ilić-Forko, J.; Vitale, L.; Miličić, D.; Abramić, M. Dipeptidyl peptidase III in malignant and non-malignant gynaecological tissue. *Eur. J. Cancer* **1998**, *34*, 399–405. doi.org/10.1016/S0959-8049(97)00401-2

Šimaga, Š.; Babić, D.; Osmak, M.; Šprem, M.; Abramić, M. Tumor cytosol dipeptidyl peptidase III activity is increased with histological aggressiveness of ovarian primary carcinomas. *Gynecol. Oncol.* **2003**, *91*, 194–200. doi: 10.1016/s0090-8258(03)00462-1

Spartan '08, Wavefunction, Inc.; Irvine, CA, USA

Špoljarić, J.; Salopek-Sondi, B.; Makarević, J.; Vukelić, B.; Agić, D.; Šimaga, Š.; Jajcanin-Jozić, N.; Abramić, M. Absolutely conserved tryptophan in M49 family of peptidases contributes to catalysis and binding of competitive inhibitors. *Bioorg. Chem.* **2009**, *37*, 70-76. https://doi.org/10.1016/j.bioorg.2009.03.002

Stewart, J.J.P. Optimization of parameters for semiempirical methods I. Method. *J. Comput. Chem.* **1989**, 10, 209-220. https://doi.org/10.1002/jcc.540100208

Tetko, I.V.; Gasteiger, J.; Todeschini, R.; Mauri, A.; Livingstone, D.; Ertl, P.; Palyulin, V.A.; Radchenko, E.V.; Zefirov, N.S.; Makarenko, A.S.; Tanchuk, V.Y.; Prokopenko V.V. Virtual computational chemistry laboratory-Design and description. *J. Comput. Aided Mol. Des.* **2005**, 19, 453-463. https://doi.org/10.1007/s10822-005-8694-y

Todeschini, R.; Consonni, V. Molecular Descriptors for Chemoinformatics, 2nd ed.; Wiley-VCH: Weinheim, Germany, 2009.

Todeschini, R.; Consonni, V.; Maiocchi, A. The K correlation index: Theory development and its application in chemometrics. *Chemom. Intell. Lab. Syst.* **1999**, 46, 13-29. https://doi.org/10.1016/S0169-7439(98)00124-5

Tomić, A.; Berynskyy, M.; Wade, R. C.; Tomić, S. Molecular simulations reveal that the long range fluctuations of human DPP III change upon ligand binding. *Mol. Biosyst.* **2015**, *11*, 3068-3080.

Tomić, A.; Gonzalez, M.; Tomić, S. The large scale conformational change of the human DPP III - substrate prefers the "closed" form. *J. Chem. Inf. Model.* **2012**, *52*, 1583–1594. doi: 10.1021/ci300141k

Tomić, A.; Horvat, G.; Ramek, M.; Agić, D.; Brkić, H.; Tomić, S. New Zinc Ion Parameters Suitable for Classical MD Simulations of Zinc Metallopeptidases. *J. Chem. Inf. Model.* **2019**. *59*, 3437–3453. https://doi.org/10.1021/acs.jcim.9b00235

Tomić, A.; Tomić, S. demystifying dpp iii catalyzed peptide hydrolysis-computational study of the complete catalytic cycle of human DPP III catalyzed tynorphin hydrolysis. *Int. J. Mol. Sci*. **2022**, 23, 1858. https://doi.org/10.3390/ijms23031858

Tomić, A.; Tomić, S. Hunting the human DPP III active conformation: combined thermodynamic and QM/MM calculations. *Dalton Trans.* **2014**, *43*, 15503–15514. doi: 10.1039/c4dt02003k

Trott, O.; Olson, A.J. AutoDock Vina: improving the speed and accuracy of docking with a new scoring function, efficient optimization, and multithreading. *J. Comput. Chem.* **2010**, *31*, 455-461. https://doi.org/10.1002/jcc.21334

Wang, J.; Wolf, R. M.; Caldwell, J. W.; Kollman, P. A.; Case, D. A. Development and testing of a general amber force field. *J. Comput. Chem.* **2004**, *25*, 1157-1174. https://doi.org/10.1002/jcc.20035

Zhang, H; Yamamoto, Y.; Shumiya, S.; Kunimatsu, M.; Nishi, K.; Ohkubo, I.; Kani, K. Peptidases play an important role in cataractogenesis: An immunohistochemical study on lenses derived from shumiya cataract rats. *Histochem. J.* **2001**, 33, 511-521. doi.org/10.1023/A:1014943522613

Zhang, S.; Lv, S.; Fu, X.; Han, L.; Han, W.; Li, W. Molecular Dynamics Simulations Study of the Interactions between Human Dipeptidyl-Peptidase III and Two Substrates. Molecules 2021, 26, 6492. https://doi.org/10.3390/molecules26216492